Journal of Constructional Steel Research 151 (2018) 263–279

Contents lists available at ScienceDirect

Journal of Constructional Steel Research

Flexural behaviour of concrete filled tubular flange girders

R. Al-Dujele, K.A. Cashell *, S. Afshan

Dept of Civil and Environmental Engineering, Brunel University London, Kingston Lane, London, Uxbridge UB8 3PH, UK

ARTICLE INFO

Article history:
Received 10 August 2018
Received in revised form 13 September 2018
Accepted 15 September 2018
Available online xxxx

ABSTRACT

In this paper, the behaviour of concrete filled tubular flange girders (CFTFGs) is investigated through both numerical and analytical modelling. These are new and complex members and their behaviour is governed by a number of inter-related parameters. This work aims to study the relative influence of a number of these variables on the flexural behaviour, particularly for CFTFGs with stiffened webs. A nonlinear three-dimensional finite element (FE) model is developed in the ABAQUS software and is validated using available experimental data. The validated model is then employed to conduct parametric studies and investigate the influence of the most salient parameters. For comparison purposes, and to observe the effect of the concrete infill, steel tubular flange girders (STFGs) with a hollow flange are also studied. The finite element models consider the effects of initial geometric imperfections, as well as other geometrical and material nonlinearities, on the response. In addition, simplified analytical expressions for the flexural capacity are proposed, and the results are compared to those from the FE analyses. It is found that CFTFGs and STFGs with the same dimensions have similar buckling shapes but different buckling loads, with the CFTFG offering greater buckling resistance. This highlights the influence of the concrete infill which increases the stiffness of the upper flange, and hence allows the member to carry additional bending moments compared to STFGs. The proposed analytical expressions, which are suitable for design, are also shown to be capable of providing an accurate depiction of the behaviour and bending moment capacity.

1. Introduction

Concrete filled tubular flange girders (CFTFGs) are I-shaped steel beams that use a hollow structural section as the compression flange which is filled with concrete and a flat plate as the tension flange. Hollow sections exhibit high torsional and compressive resistance when compared with open sections. Therefore, employing a tubular flange as the compression flange in CFTFG, the resulting sections have been shown to offer substantially higher torsional stiffness compared with conventional steel I-beams of similar depth, width and weight [1]. This results in increases in the lateral-torsional buckling resistance of these members which, in turn, leads into a reduction in lateral bracing requirements for CFTFGs. Hence, several researchers have investigated the use of concrete filled tubular flange girders in structural applications, such as bridges, car parks and multi-storey buildings.

A number of researchers have investigated the behaviour of hollow flange beams in recent years including triangular hollow flange beams (THFBs), LiteSteel beams (LSBs) and hollow tubular flange plate girders (HTFPGs), as presented in Fig. 1. Pi and Trahair conducted pioneering studies in to lateral-distortional buckling of triangular hollow flange beams and a simple expression was proposed to define the effect of web distortion on the flexural strength of these members under uniform bending [2]. Avery and Mahendran [3] concluded that including transverse stiffeners on the web of hollow flange beams significantly improves the lateral buckling flexural strength of the member. LiteSteel beams (LSBs) are a relatively new structural form, typically made from cold-formed steel in a channel shape but with rectangular hollow flanges as presented in Fig. 1(b), and these have been studied recently in Australia [4,5]. Hollow tubular flange plate girders (HTFPGs) with a slender web, as shown in Fig. 1(c), have also been proposed and investigated [6–9]. In these studies, the shear strength of homogeneous and hybrid HTFPGs was examined, where hybrid girders are sections which use different materials for the web and flanges, as well as the buckling behaviour of members with slender stiffened or un-stiffened webs. It was noted that HTFPGs are still sensitive to lateral-distortional buckling even with the hollow flanges although they can resist much higher critical loads than conventional I-beams.

For hollow flange plate girders, it has been generally noted that members with a relatively thin tube thickness are susceptible to local buckling of the compression tubular flange, which limits the flexural resistance of the cross-section. To overcome this, concrete filled tubular flange girders (CFTFGs) have been proposed and investigated by a number of researchers. Early studies at Lehigh University in the USA tested two 18 m long CFTFGs with a rectangular concrete filled tube as the compression flange and a flat plate as the tension flange, as depicted in Fig. 2(a) [10,11]. Kim and Sause [12] studied the performance of CFTFGs with a circular concrete filled tube as the compression flange

* Corresponding author.
E-mail address: katherine.cashell@brunel.ac.uk (K.A. Cashell).

https://doi.org/10.1016/j.jcsr.2018.09.017
0143-974X/

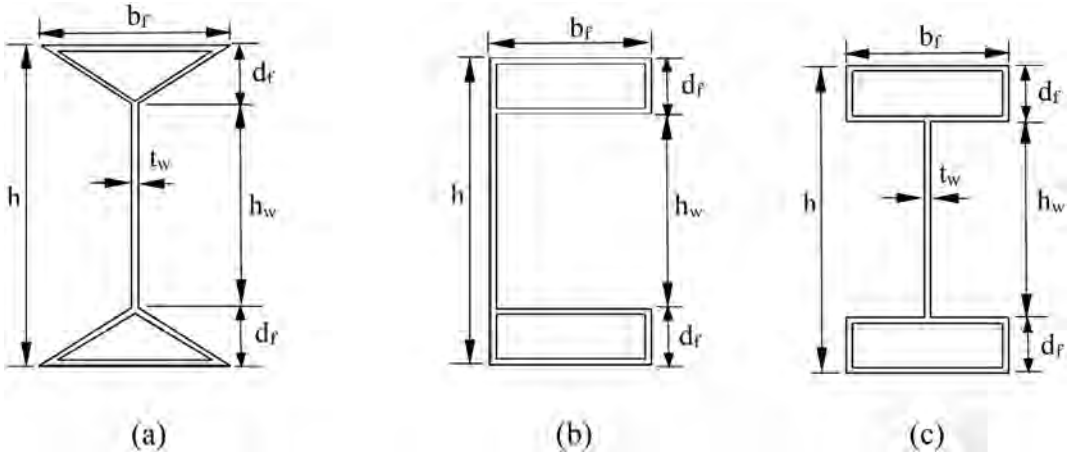

Fig. 1. Hollow flange girders including (a) triangular hollow flange beam, (b) LiteSteel beam and (c) rectangular hollow tubular flange plate girder.

rather than a rectangle, as illustrated in Fig. 2(b). Some of the potential benefits of CFTFGs were summarized, including the provision of more strength, stiffness, and stability compared with a flat plate flange which uses a similar amount of steel or a hollow flange, and design formulas for predicting the lateral-torsional buckling (LTB) strength of CFTFGs were proposed. Other shapes have also been studied including beams with a pentagonal top flange filled with concrete [13], as shown in Fig. 2(c), and CFTFGs which are curved along the length [14]. Generally, for the many different configurations which have been studied, it has been shown that CFTFGs bring numerous advantages compared with conventional steel girders, particularly for large spanning or heavily loaded applications, including the ability to minimize the required under-clearance, simplify erection, and eliminate the need for stiffeners, cross frames or diaphragms.

In this paper, the flexural behaviour of circular concrete filled tubular flange girders (CFTFGs) and circular steel tubular flange girders (STFGs) is investigated through numerical modelling. The paper begins with a description of the finite element (FE) model which was validated against the test data available in the literature [15], following which, parametric studies were conducted to investigate the effect of key parameters such as the size of the tube diameter (D_{tube}), the ratio of D_{tube} to the tube thickness, the thickness of the bottom flange, the web plate slenderness, the aspect ratio of the web panel and also the material strengths. Based on the analysis, as well as a fundamental assessment of the behaviour, a series of analytical expressions which are suitable for design are presented and assessed for predicting the bending capacity of circular CFTFGs.

2. Numerical modelling

2.1. General

The finite element analysis package ABAQUS [16] was employed to examine the ultimate moment capacity of simply supported CFTFGs, taking into account the geometrical and material nonlinearities. The numerical models contained an initial geometric imperfection which was generated by means of the first buckling mode shape of a perfect beam (i.e. perfectly straight and constant geometry) multiplied by an amplitude factor. For this purpose, an elastic eigenvalue buckling analysis was first conducted, and then the first buckling mode shape of the beam with an imperfection amplitude of L/1000, where L is the beam length, was imported to the nonlinear model as the starting geometry. The global imperfection amplitude was taken as L/1000 in accordance with the permitted out-of-straightness tolerance in EN 1090-2 [17]

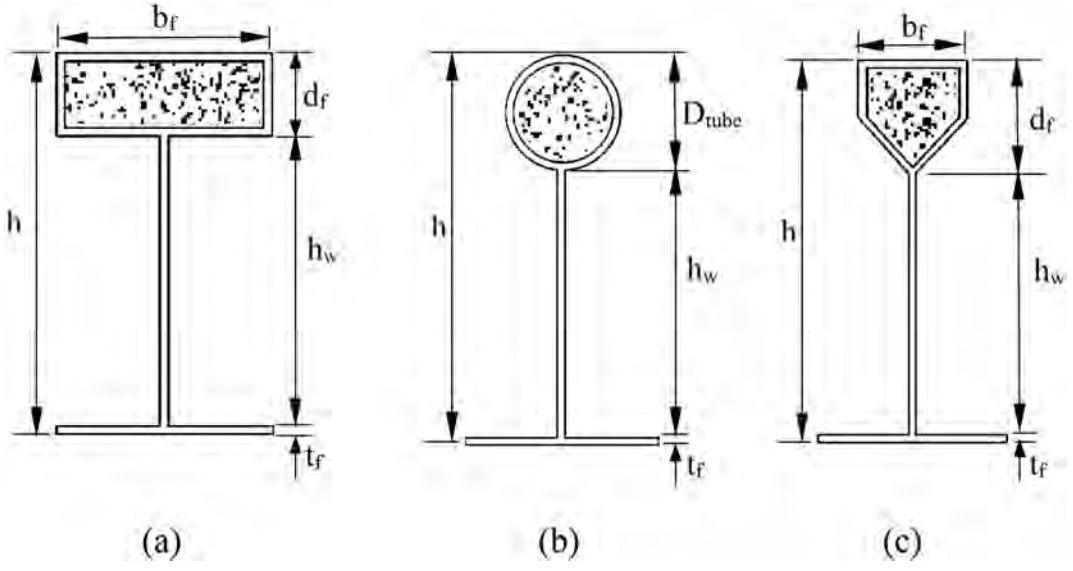

Fig. 2. Girders with concrete filled tubular flanges inlcuding (a) rectangular flange, (b) circular flange and (c) pentagonal flange.

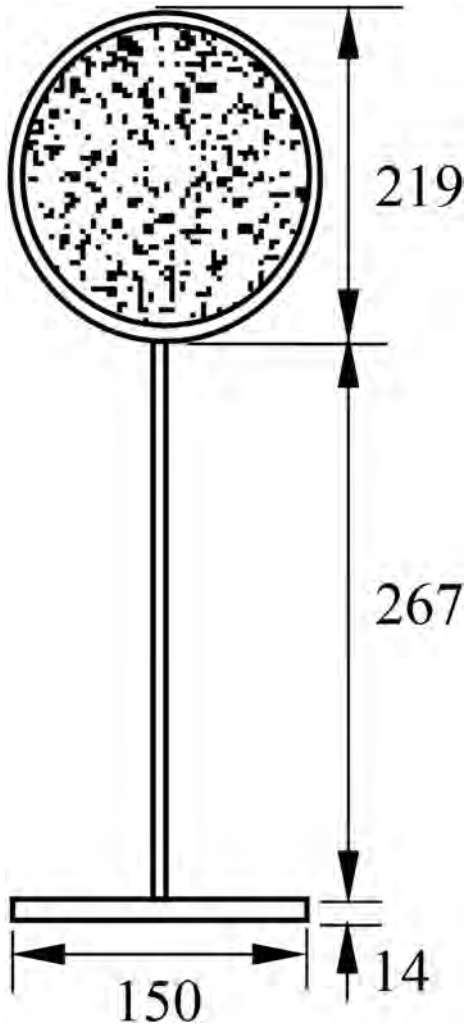

Fig. 3. Cross-section of a composite beam with a concrete filled circular tubular flange (all units in mm).

and the AISC [18,19], and has been used by other researchers in similar studies e.g. [20,21]. The implicit dynamic analysis method in ABAQUS was used to solve the geometrically and materially nonlinear problem, where the load was applied incrementally and the nonlinear geometry parameter (*NLGEOM, in the ABAQUS) was included to allow for changes in the geometry under load. This nonlinear dynamic analysis method uses an implicit time integration scheme to determine the quasi-static response of the system, which was found in the current study to provide the best convergence behaviour owing to the high energy dissipation associated with quasi-static applications during certain stages of the loading history.

2.2. Details of validation model

The specimen details incorporated in the validation FE model are based on the circular tubular flange girder which was examined in the test programme of Wang et al. [15]. Accordingly, the cross-section is 0.5 m in height and 4.3 m in length, as shown in Figs. 3 and 4. Table 1 presents the principal dimensions of the tests, namely D_{tube}, t_t, h_w, t_w, b_f, t_f, and $t_{stiffener}$ which represent the tube outside diameter, tube thickness, web depth, web thickness, width of the bottom flange, thickness of the bottom flange and stiffener thickness, respectively. The beam is subjected to two concentrated loads in the vertical direction on the top surface and the distance between the loading points is 1 m. There are four stiffeners along the beam length, as shown in Fig. 4, and each has a thickness of 12 mm. These are located at the supports and loading points in order to prevent local instability of the web at these locations. Simply supported boundary conditions in the tests were simulated in the FE model by restraining suitable displacement and rotational degrees of freedom at the beam ends. The steel section was made from Q235 steel, and the material properties incorporated in the model are presented in Table 2 including the yield strength f_y, ultimate strength f_u, Young's modulus (E) and Poisson's ratio [22]. Also included in the Table 2 are the compressive strength f_c and Poisson's ratio of the concrete.

Table 1
Dimensions of the CFTFG cross-section.

D_{tube} (mm)	t_t (mm)	h_w (mm)	t_w (mm)	b_f (mm)	t_f (mm)	$t_{stiffener}$ (mm)
219	8	267	6	150	14	12

Table 2
Details of the material properties.

Steel [20]				Concrete [22]	
Yield stress, f_y (N/mm^2)	Ultimate stress, f_u (N/mm^2)	Young's modulus, E (N/mm^2)	Poisson's ratio	Compressive cylinder strength of concrete, f_c (MPa)	Poisson's ratio
287.9	430.2	195,000	0.28	38.6	0.20

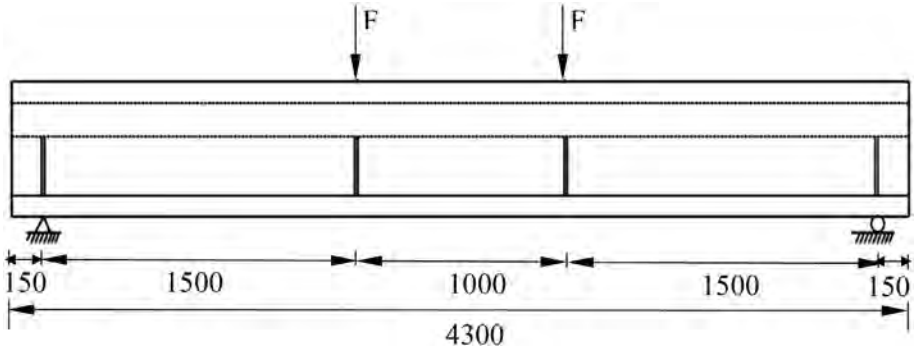

Fig. 4. Schematic of the simply supported beam (all units in mm).

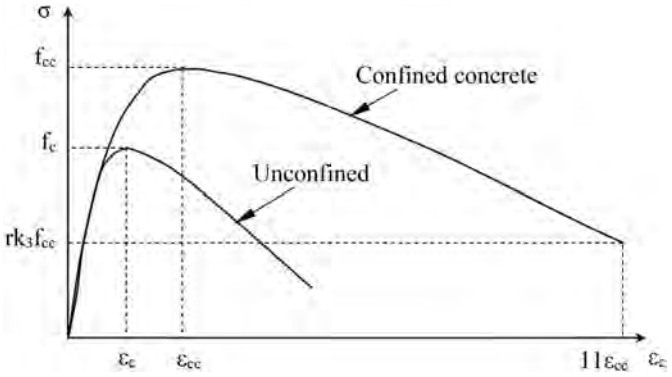

Fig. 5. Typical stress-strain curve of confined and unconfined concrete (reproduced from [23]).

2.3. Material modelling

2.3.1. Concrete

The stress-strain relationship of unconfined concrete is shown in Fig. 5, where f_c is the unconfined ultimate cylinder compressive strength of concrete, ε_c is the corresponding strain at f_c which is determined (as a percentage) as given by Eq. (1) in accordance with Eurocode 2 Part 1–1 [23].

$$\varepsilon_c = 0.7(f_c)^{0.31} \leq 2.8 \tag{1}$$

When the concrete filled steel tube is exposed to axial compression, a gap occurs between the steel tube and the concrete core in the elastic range because Poisson's ratio for the concrete is smaller than that of the steel tube. Beyond the elastic range, the inner concrete dilates (strains transversely) at a higher/faster rate than the steel tube, hence making contact between the steel tube and the concrete to develop again. As the axial compressive stress increases further, continued dilation of the concrete core is restricted by the steel tube, generating a variable confining pressure in the concrete in the transverse direction. This confining pressure effectively increases the compressive strength of the concrete core. In a CFTFG, the concrete is confined by the circular steel tube section, which results in increased ductility and strength of the concrete core, compared to unconfined concrete.

In the current study, the stress-strain response of confined concrete proposed by Hu et al. [24] is adopted in the numerical simulations. This approach has been adopted by other researchers for the simulation of concrete filled tubular columns which are eccentrically loaded, leading to non-uniform confining pressure, as occurs in the current scenario [25,26]. Typical uniaxial stress–strain curves of unconfined concrete is shown in Fig. 5, where f_{cc} and ε_{cc} are the uniaxial compressive strength and the corresponding strain of confined concrete, respectively. Mander et al. [27] proposed relationships between confined and unconfined concrete strength and strain values, as given by Eqs. (2)and(3), respectively.

$$f_{cc} = f_c + k_1 fl \tag{2}$$

$$\varepsilon_{cc} = \varepsilon_c\left(1 + k_2\frac{fl}{f_c}\right) \tag{3}$$

Values of 4.1 and 20.5 are used for k_1 and k_2, respectively, based on the study of Richart et al. [28]. The term 'fl' denotes the confining pressure in the concrete, which is determined in the current study based on the empirical relationships presented in Eqs. (4) and (5) proposed in [24].

$$fl/f_y = 0.043646 - 0.000832(D_{tube}/t_t) \quad \text{for} \quad 21.7 \leq D_{tube}/t_t \leq 47 \tag{4}$$

$$fl/f_y = 0.006241 - 0.000357(D_{tube}/t_t) \quad \text{for} \quad 47 \leq D_{tube}/t_t \leq 150 \tag{5}$$

The stress-strain curve of confined concrete, as presented in Fig. 5, consists of three parts. Initially, it is assumed that the confined concrete responds linearly, obeying Hooke's law, and this continues up to around 40% of compressive strength in the ascending branch [23,29]. During this phase of the response, the behaviour of confined and unconfined concrete is identical, as shown in Fig. 5. The initial Young's modulus (in GPa) can be estimated with reasonable accuracy from the empirical formulation provided in Eurocode 2 [23] given in Eq. (6).

$$E_{cc} = 22 \times (f_c/10)^{0.3} \tag{6}$$

The second part of the stress-strain curve defines the nonlinear behaviour before the concrete reaches its maximum strength, starting from the proportional limit ($0.4f_c$) to the maximum confined concrete strength f_{cc}. The relationship of concrete stress σ_c and strain ε in this part of the response was proposed by Saenz [30], and is as described by Eqs. (7)–(9)

$$\sigma_c = \frac{E_{cc}\varepsilon}{1 + (R + R_E - 2)\left(\frac{\varepsilon}{\varepsilon_{cc}}\right) - (2R-1)\left(\frac{\varepsilon}{\varepsilon_{cc}}\right)^2 + R\left(\frac{\varepsilon}{\varepsilon_{cc}}\right)^3} \tag{7}$$

where:

$$R_E = \frac{E_{cc}\varepsilon_{cc}}{f_{cc}} \tag{8}$$

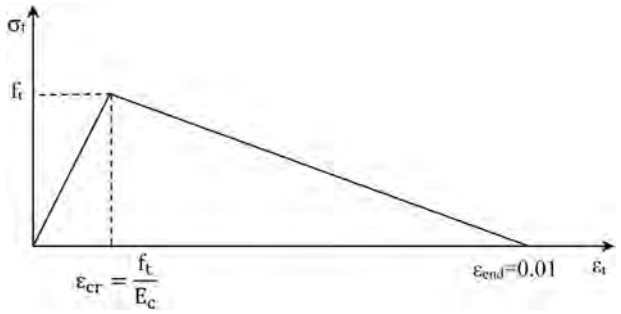

Fig. 6. Tensile stress-strain curve for concrete.

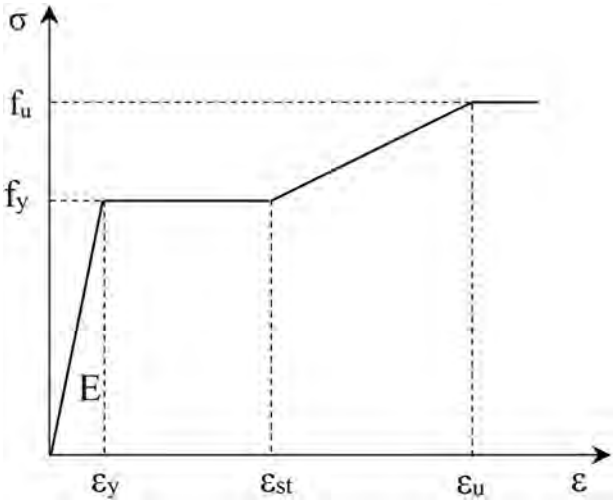

Fig. 7. Stress–strain curve of steel beam (reproduced from [21]).

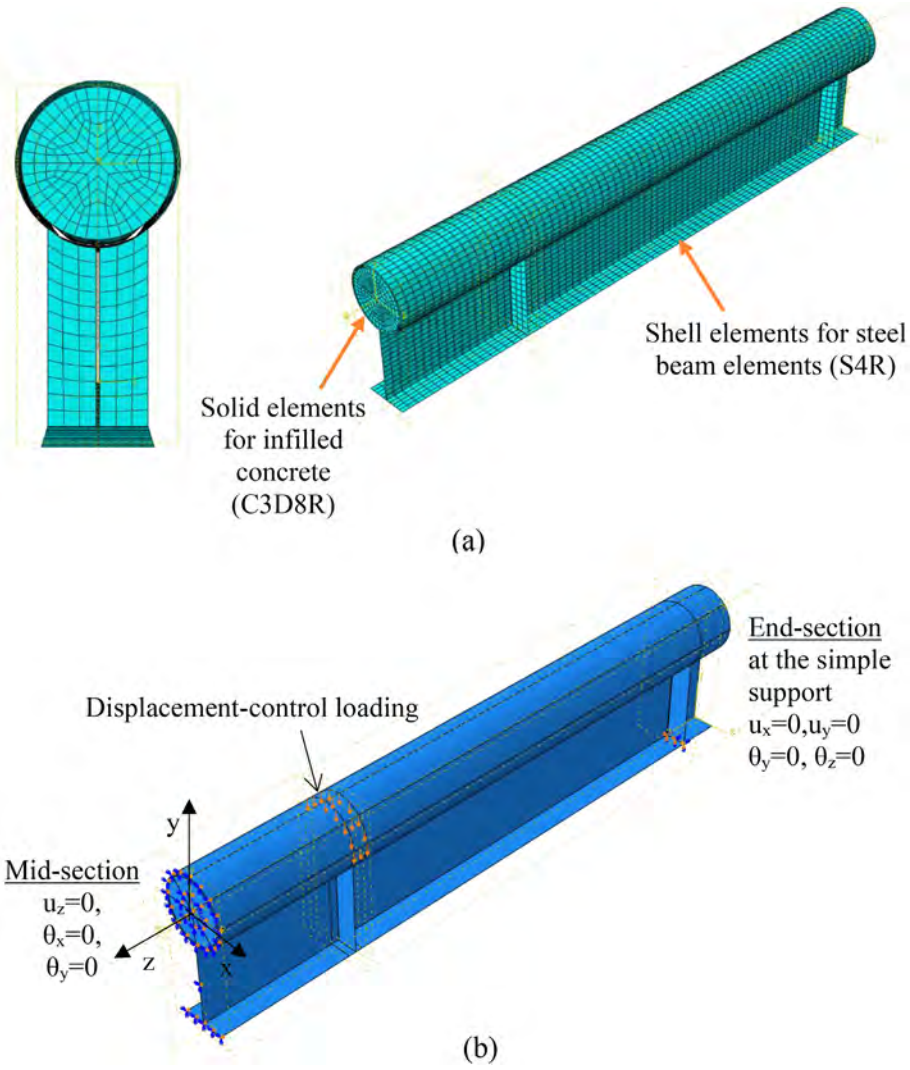

Fig. 8. FE model for the CFTFG, including (a) finite element mesh and (b) support and loading conditions.

and

$$R = \frac{R_E(R_\sigma - 1)}{(R_\varepsilon - 1)^2} - \frac{1}{R_\varepsilon} \tag{9}$$

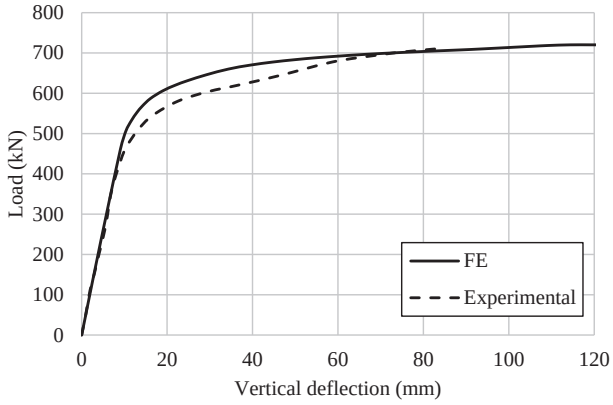

Fig. 9. Load versus deflection relationship from the FE analysis and experimental results.

where R_ε and R_σ were both assumed to be 4.0, in accordance with the recommendations in [31].

The third and last part of the curve is the descending branch which begins at the maximum confined concrete strength f_{cc} and decreases linearly until a stress of $f_{c,u}$ is reached at a corresponding strain of $\varepsilon_{c,u}$, which are determined as given in Eqs.(10) and (11), respectively.

$$f_{c,u} = rk_3 f_{cc} \tag{10}$$

$$\varepsilon_{c,u} = 11\varepsilon_{cc} \tag{11}$$

where the value of the parameter k_3 for concrete filled circular steel tubes is calculated using Eq. (12), based on the recommendations presented in [24].

$$k_3 = 1 \quad \text{for} \quad 21.7 \le D_{tube}/t_t \le 40$$
$$k_3 = 0.0000339\left(\frac{D_{tube}}{t_t}\right)^2 - 0.010085\left(\frac{D_{tube}}{t_t}\right) + 1.3491 \quad \text{for} \quad 40 \le D_{tube}/t_t \le 150 \tag{12}$$

As a result of the experimental studies carried out by Giakoumelis and Lam in 2004 [32], it was proposed in [33,34] that the parameter r may be taken as 1.0 for concrete with cube strength of 30 MPa and 0.5

Table 3
Comparisons of numerical, experimental and analytical ultimate strengths.

$P_{u,Exp}$ (kN)	$M_{u,Exp}$ (kNm)	$P_{u,FE}$ (kN)	$M_{u,FE}$ (kNm)	$M_{u,FE}/M_{u,Exp}$	PNA location, y_1 (mm)	$M_{u,Calc}$ (kNm)	$M_{u,FE}/M_{u,Calc}$	$M_{u,Exp}/M_{u,Calc}$
716.0	537.0	720.2	540.2	1.006	155.9	544.6	0.992	0.986

for concrete with a cube strength of 100 MPa and linear interpolation can be used for intermediate values.

In the ABAQUS FE model, the concrete infill is represented using 8-noded brick elements with reduced integration, known as C3D8R in the ABAQUS library. The concrete damaged plasticity (CDP) model is employed for modelling the constitutive behaviour of the concrete, based on the relationships described before. The model assumes that the infilled concrete fails either in compression, through crushing, or tension, through cracking. In addition to the compressive and tensile constitutive relationships, a number of other parameters are required in the CDP model, including the dilation angle, flow potential eccentricity and viscosity parameter which are assigned values of 36°, 0.1, and 0, respectively, as used by other researchers [35]. The ratio of the strength in the biaxial state to the strength in the uniaxial state, f_{b0}/f_c, is taken as 1.16 whilst the ratio of the second stress invariant on the tensile meridian (K) is given a value of 0.667 in the present analysis.

In addition, the compressive damage parameter d_c needs to be defined at each inelastic strain level. It ranges from zero, for undamaged material, to unity, when the material can no longer sustain any load. The value for d_c is found only for the descending branch of the stress-strain curve of concrete in compression, as given by Eqs. (13) and (14).

$$d_c = 0 \qquad \text{when } \varepsilon_c < \varepsilon_{cc} \tag{13}$$

$$d_c = \frac{f_{cc} - \sigma_c}{f_{cc}} \qquad \text{when } \varepsilon_c \geq \varepsilon_{cc} \tag{14}$$

In this study, it was assumed that after the tensile strength of concrete f_t at corresponding strain of ε_{cr} has been reached, the tensile strength decreases linearly to reach zero stress at a total tensile strain at the end ε_{end} of 0.01, as shown in Fig. 6. The tensile strength of concrete f_t, according to Eurocode 2 [23], is taken from Eqs. (15) and (16).

$$f_t = 0.3 f_c^{2/3} \qquad \text{for} \qquad f_c \leq 50\ \text{N/mm} \tag{15}$$

$$f_t = 2.12\ \ln(1 + 0.1 f_c) \qquad \text{for} \qquad f_c > 50\ \text{N/mm}^2 \tag{16}$$

Similar to the simulation of concrete in compression in the CDP model, the tensile damage parameter d_t, which is valid only in the descending branch of the stress-strain curve for concrete in tension, is defined at each increment of cracking strain, as described by Eqs. (17) and (18) follows:

$$d_t = 0 \qquad \text{for} \qquad \varepsilon_t < \varepsilon_{cr} \tag{17}$$

$$d_t = \frac{f_t - \sigma_t}{f_t} \qquad \text{for} \qquad \varepsilon_t \geq \varepsilon_{cr} \tag{18}$$

2.3.2. Steel

The steel employed in the tested beam which is used later for validation is Q235 steel with nominal yield stress and ultimate tensile stress of 287.9 and 430.2 MPa, respectively [22]. An idealised tri-linear stress–strain relationship is assumed to model the steel material in the FE model, as shown in Fig. 7, where f_y and ε_y are the yield stress and strain, respectively, ε_{st} is the strain at the onset of strain hardening and f_u and ε_u are the ultimate tensile stress and strain at ultimate tensile stress, respectively. The key values used in the model are presented in Table 2. The strain at the onset of strain hardening ε_{st} and the strain at the ultimate tensile stress ε_u are taken as 0.025 and 0.2, respectively [36]. The engineering stress–strain (σ_{eng}-ε_{eng}) curve is converted to true stress–strain (σ_{true}-ε_{true}) curve for the ABAQUS model using Eqs.(19) and (20), respectively.

$$\varepsilon_{true} = \ln(1 + \varepsilon_{eng}) \tag{19}$$

$$\sigma_{true} = \sigma_{eng}(1 + \varepsilon_{eng}) \tag{20}$$

The top tubular flange, web, bottom flange and stiffeners are all modelled using the four-noded, three-dimensional shell element with reduced integration (S4R in the ABAQUS library). The S4R element has six active degrees of freedom per node, including three displacements and three rotations. The reduced integration enables more efficient computation without compromising the accuracy of the results. A tie contact is defined between the surface of the steel section and the

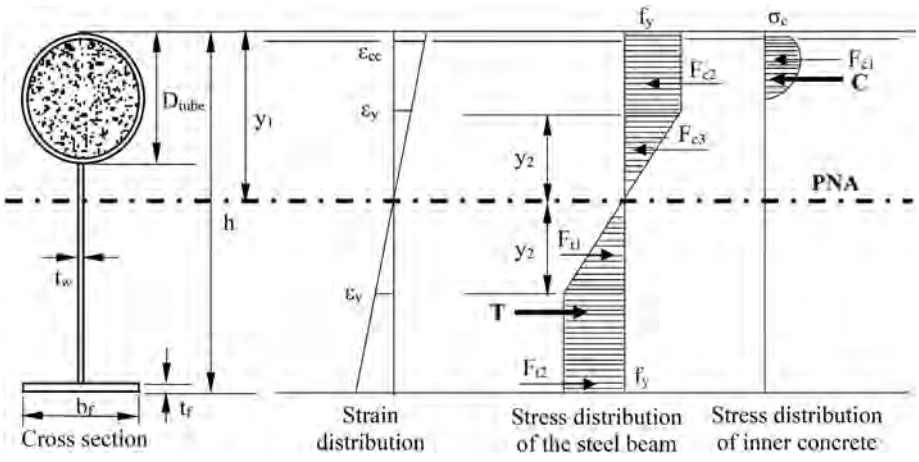

Fig. 10. Distributions of strain and stress for Case 1, where the PNA is in the web of the steel section ($y_1 > D_{tube}$).

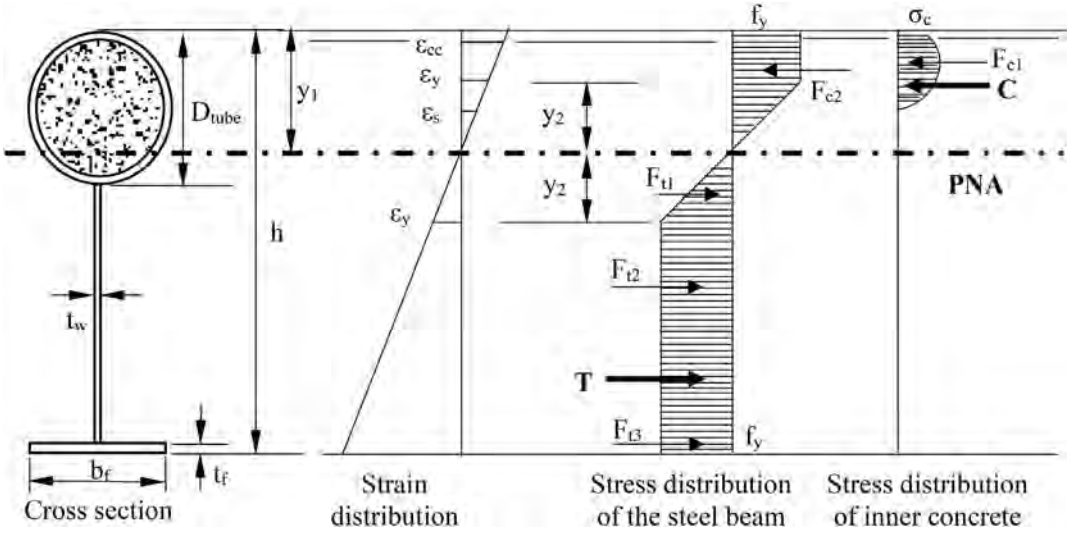

Fig. 11. Distributions of strain and stress for Case 2, where the PNA is in the tubular flange section ($y_1 < D_{tube}$).

edges of the stiffeners. Following a mesh sensitivity study, it has been found that an element size of 30 × 30 mm provides the best combination of accuracy and computational efficiency and therefore is applied to all elements in the model. The finite element mesh of a typical specimen is presented in Fig. 8(a).

2.4. Support and loading conditions

The geometry and loading conditions of the beam are symmetrical about the mid-span and therefore only half the girder length is modelled. Accordingly, one end section of the beam model has simply supported boundary conditions whilst the other end has symmetrical boundary conditions, as shown in Fig. 8(b), in which u_x, u_y, u_z, θ_x, θ_y, and θ_z are the displacements and the rotations about the global x, y and z axes, respectively. The y-z plane is considered to be in-plane whilst the x-z and x-y planes are out-of-plane, in the current study. At the end of the beam (i.e. at the support), the vertical u_y and lateral displacements u_x of all nodes along the y-axis (i.e., when $x = 0$), and the twist rotations about z and y-axes (θ_z and θ_y) are restrained against movement and therefore assigned values equal to zero. At the middle of the beam, the longitudinal displacements u_z and rotations about the x and y-axes (θ_x and θ_y) are also restrained against all movement. The loading is applied to the top surface of the beam in displacement control through two concentrated loads along the full length or one loading point when half the span is considered.

2.5. Validation of the load-displacement response

To assess the accuracy of the load-displacement response generated by the FE model, the test conducted by Wang et al. [15] was simulated as described in previous sections. This is the only test which has been done on concrete filled tubular flange girders with a circular top flange, to date, in the public domain. The load-displacement response of the CFTFG from both the FE model and the experimental programme is presented in Fig. 9. The ultimate load and ultimate moment obtained from the FE analyses – $P_{u,FE}$ and $M_{u,FE}$, respectively are compared with the test ultimate load and ultimate moment – $P_{u,Exp}$ and $M_{u,Exp}$, respectively in Table 3. From Fig. 9, it is clear that the FE model is capable of providing a good representation of the general response and also offers an excellent prediction of the ultimate load and moment of the CFTFG. Residual stresses are not incorporated in the FE model as it has been shown that they can be neglected for short unbraced members which are < 20 m in length [37].

In terms of the general behaviour, and with reference to Fig. 9, it can be observed that the response predicted by the FE model is divided into four phases. Firstly, below a load of around 400 kN, there is a linear relationship between load and displacement in the elastic phase, and the response is very well predicted by the model in this range. Secondly, when the load reaches 500–600 kN, the behaviour becomes nonlinear. With the expansion of the yielded region from the bottom flange to the middle of the steel section, the flexural rigidity decreases and the

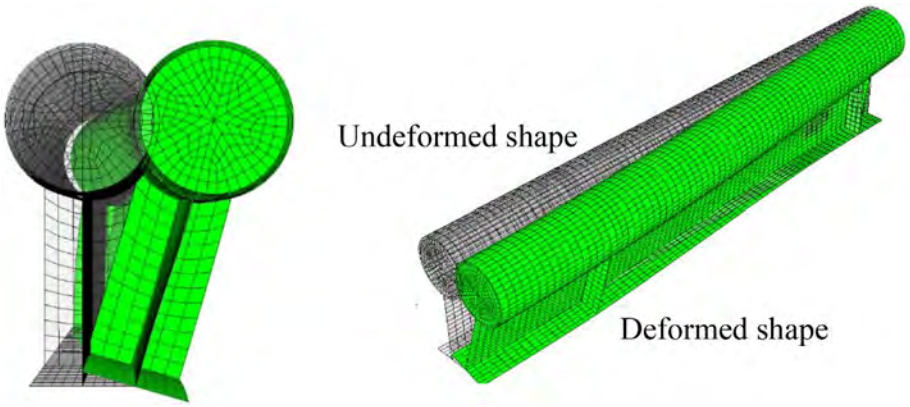

Fig. 12. View of the finite element model in both the deformed and undeformed shapes.

Table 4
Details of CFTFGs with different tube diameters.

CFTFG Group	Specimen	Geometric details					$M_{u,FE}$	$M_{u,Calc}$	PNA location, y_1	$M_{u,FE}/M_{u,Calc}$
		L	D_{tube}	h_w	a/h_w	t_f				
		(mm)	(mm)	(mm)		(mm)	(kNm)	(kNm)	(mm)	
G1	GR1	4300	180	267	5.62	14	439.7	454.3	137.1	0.968
	GR2					28	650.5	667.2	152.4	0.975
	GR3			500	3	14	744.0	758.4	146.7	0.981
	GR4					28	1010.8	1023.7	166.3	0.987
G2	GR5		200	267	5.62	14	482.1	494.6	146.8	0.975
	GR6					28	703.1	717.2	160.9	0.980
	GR7			500	3	14	793.5	805.4	155.8	0.985
	GR8					28	1062.9	1073.5	172.6	0.990
G3	GR9		210	267	5.62	14	504.1	513.6	151.6	0.981
	GR10					28	729.9	738.1	165.2	0.989
	GR11			500	3	14	818.8	824.5	160.4	0.993
	GR12					28	1089.5	1094.9	176.3	0.995
G4	GR13		219	267	5.62	14	540.2	544.6	155.9	0.992
	GR14					28	754.9	760.3	169.2	0.993
	GR15			500	3	14	842.5	845.9	164.4	0.996
	GR16					28	1117.1	1121.2	179.7	0.996
G5	GR17		300	267	5.62	14	730.3	735.8	189.7	0.992
	GR18					28	1002.4	1008.7	202.2	0.994
	GR19			500	3	14	1079.3	1082.4	197.8	0.997
	GR20					28	1366.0	1363.7	211.4	0.999

stress redistributes. In this elastic-plastic stage, there are some disparities between the experimental and numerical curves and the model somewhat over-predicts the capacity of the beam. This difference is likely to be due to a combination of factors which affect deformations, such as the idealisation of the material nonlinearity in the FE model as well as the likelihood of initial imperfections in the real structure. In the third phase, when loading exceeds 600 kN, the displacement increases rapidly as plasticity spreads in the middle region of the beam. Finally, in the fourth phase when the load reaches around 720 kN, the response plateaus as the displacement continues to increase with very little change in the load. The failure mode observed in both the FE model and the experiment, is a combination of steel yielding and torsional buckling. Overall, the simulated load-deformation curves reflect the experimental behaviour very well. Although there is only one experiment available for validation which is not ideal, it is concluded that the FE model is capable of predicting the behaviour and strength of that member and is suitable for conducting further parametric studies on CFTFGs under bending.

3. Analytical model for flexural strength

In this section, a series of analytical expressions for predicting the bending capacity of circular CFTFGs are developed which can be used both for analysis and design of these members. The approach is based on plastic theory in which the position of the plastic neutral axis and the plastic bending moment capacity can be identified by applying the equilibrium of internal forces equations to the cross-section. An equivalent rectangular and triangular stress block is assumed for the concrete (as shown in Fig. 10 and discussed hereafter) and the steel is assumed to behave in an elastic-perfectly plastic manner. The confining effect provided by the steel tube on the concrete infill is considered in the analytical model.

Table 5
Details of STFGs with different tube diameters.

STFG Group	Specimen	Geometric details					$M_{u,FE}$	$M_{u,Calc}$	PNA location, y_1	$M_{u,FE}/M_{u,Calc}$
		L	D_{tube}	h_w	a/h_w	t_f				
		(mm)	(mm)	(mm)		(mm)	(kNm)	(kNm)	(mm)	
G6	GR21	4300	180	267	5.62	14	342.9	357.7	157.6	0.959
	GR22					28	490.1	505.3	303.3	0.970
	GR23			500	3	14	615.9	629.4	244.8	0.979
	GR24					28	806.4	815.5	419.8	0.989
G7	GR25		200	267	5.62	14	348.4	361.1	151.8	0.965
	GR26					28	499.4	513.0	281.4	0.973
	GR27			500	3	14	613.3	625.7	222.9	0.980
	GR28					28	833.0	840.8	397.9	0.991
G8	GR29		210	267	5.62	14	379.5	392.2	146.8	0.968
	GR30					28	548.9	562.7	270.3	0.976
	GR31			500	3	14	633.1	645.2	211.9	0.981
	GR32					28	875.2	882.6	386.8	0.992
G9	GR33		219	267	5.62	14	391.2	400.8	140.0	0.976
	GR34					28	569.0	580.7	260.6	0.980
	GR35			500	3	14	650.8	663.4	202.1	0.981
	GR36					28	905.8	911.1	377.1	0.994
G10	GR37		300	267	5.62	14	492.8	498.8	114.8	0.988
	GR38					28	665.9	672.2	171.9	0.991
	GR39			500	3	14	756.2	760.5	142.7	0.994
	GR40					28	1173.5	1175.4	288.4	0.998

Table 6
Details of CFTFGs with different tube thicknesses.

CFTFG Group	Specimen	Geometric details							$M_{u,FE}$	M_{uCalc}	PNA location, y_1	$M_{u,FE}/M_{u,Calc}$
		L	D_{tube}	h_w	a/h_w	h_w/t_w	D_{tube}/t_t	t_f				
		(mm)	(mm)	(mm)				(mm)	(kNm)	(kNm)	(mm)	
G11	GR41	4300	219	267	5.62	44.5	43.8	14	463.2	477.3	154.2	0.970
	GR42							28	691.3	707.7	183.5	0.977
	GR43						27.4	14	540.2	544.6	155.9	0.992
	GR44							28	754.9	760.3	169.2	0.993
	GR45						21.9	14	557.2	560.7	157.6	0.994
	GR46							28	789.9	793.7	167.8	0.995
G12	GR47					26.7	43.8	14	538.1	552.7	167.8	0.974
	GR48							28	754.2	769.3	197.5	0.980
	GR49						27.4	14	599.8	603.2	164.2	0.994
	GR50							28	824.0	828.9	178.0	0.994
	GR51						21.9	14	634.7	638.3	164.3	0.994
	GR52							28	859.8	863.4	174.9	0.996
G13	GR53			500	3	83.3	43.8	14	786.4	800.8	172.7	0.982
	GR54							28	1058.3	1069.3	209.8	0.990
	GR55						27.4	14	842.5	845.9	164.4	0.996
	GR56							28	1117.1	1121.2	179.7	0.996
	GR57						21.9	14	874.3	878.7	164.2	0.995
	GR58							28	1152.8	1157.3	175.6	0.996
G14	GR59					50	43.8	14	968.7	985.2	201.5	0.983
	GR60							28	1300.3	1312.6	274.1	0.991
	GR61						27.4	14	1035.3	1039.0	179.7	0.996
	GR62							28	1377.2	1381.1	197.8	0.997
	GR63						21.9	14	1069.4	1074.5	176.2	0.995
	GR64							28	1413.2	1417.7	189.2	0.997

3.1. Location of the plastic neutral axis

In order to determine the bending capacity of the section, it is first necessary to determine the location of the plastic neutral axis (PNA). Two cases are considered in this study. Case 1 assumes that the PNA is in the web of the steel section, as shown in Fig. 10, while Case 2 assumes that the PNA is in the tubular flange, as demonstrated in Fig. 11. With reference to these figures, and in order to determine the exact location of the PNA, the following assumptions are adopted:

- If the PNA is within the concrete filled portion of the section, it is assumed the concrete below the plastic neutral axis does not contribute to the tension capacity.
- By assuming $x_0 = 0$ and $y_0 = y_1 - R$, the coordinate (x_0, y_0) is the centre of the circular tube, where R is the outer radios of the steel tube.
- The term y_2, which is the vertical height of the triangular stress block is determined by interpolating the strain distribution across the cross-section, given by:

Table 7
Details of STFGs with different tube thicknesses.

STFG Group	Specimen	Geometric details							$M_{u,FE}$	$M_{u,Calc}$	PNA location, y1	$M_{u,FE}/M_{u,\ Calc}$
		L	D_{tube}	h_w	a/h_w	h_w/t_w	D_{tube}/t_t	t_f				
		(mm)	(mm)	m)m)				(mm)	(kNm)	(kNm)	(mm)	
G15	GR65	4300	219	267	5.62	44.5	43.8	14	292.9	306.9	247.4	0.954
	GR66							28	308.9	322	422.4	0.959
	GR67						27.4	14	391.2	400.8	140	0.976
	GR68							28	569.0	580.7	260.6	0.980
	GR69						21.9	14	435.1	444.9	107.6	0.978
	GR70							28	604.9	613.6	155.3	0.986
G16	GR71					26.7	43.8	14	301.4	310.1	289.4	0.972
	GR72							28	314.2	322.9	394.4	0.973
	GR73						27.4	14	431.1	443.6	192.7	0.972
	GR74							28	557.9	572.1	297.4	0.975
	GR75						21.9	14	480.8	488.2	129.1	0.985
	GR76							28	643.1	648.9	234.2	0.991
G17	GR77			500	3	83.3	43.8	14	334.9	343.4	363.7	0.976
	GR78							28	396.1	404.9	538.9	0.978
	GR79						27.4	14	650.8	663.4	202.1	0.981
	GR80							28	905.8	911.1	377.1	0.994
	GR81						21.9	14	718.6	726.9	116.8	0.988
	GR82							28	946.4	952.6	271.4	0.994
G18	GR83					50	43.8	14	360.3	368	405.9	0.979
	GR84							28	428.2	436.3	510.7	0.981
	GR85						27.4	14	722.3	735.6	308.9	0.982
	GR86							28	942.7	954.6	413.8	0.988
	GR87						21.9	14	840.3	848.6	245.6	0.990
	GR88							28	1029.9	1034.8	350.7	0.995

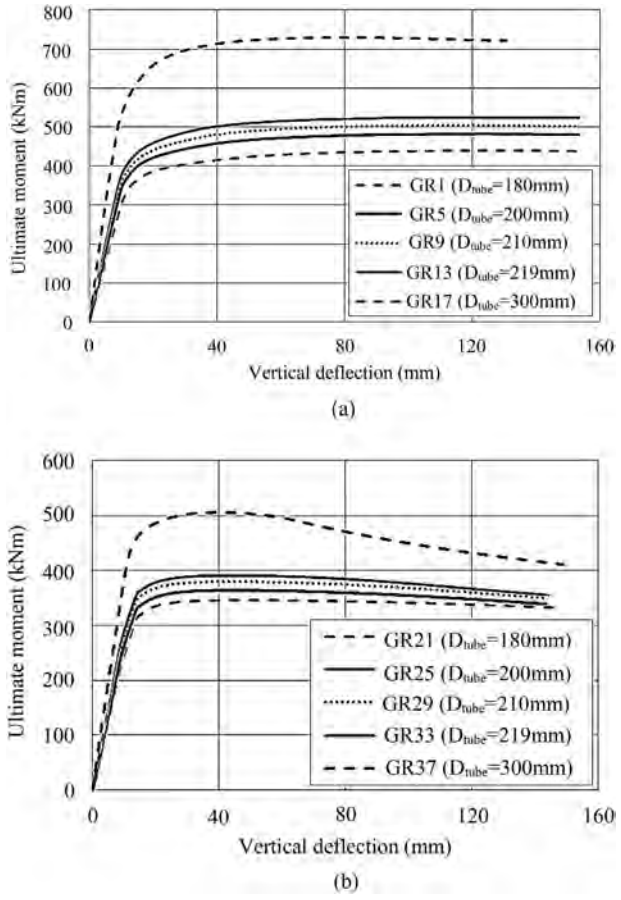

Fig. 13. Ultimate moment versus deflection responses for (a) CFTFGs (b) STFGs with different tube diameters.

$$\frac{\varepsilon_{cc}}{y_1-t_t}=\frac{\varepsilon_y}{y_2}\rightarrow y_2=\frac{\varepsilon_y}{\varepsilon_{cc}}(y_1-t_t).$$

- In the triangular stress block, where the steel is behaving in an elastic manner (i.e. $f_s=\varepsilon_s E$, where f_s and ε_s are the stress and strain in the steel section, respectively, and E is the elastic modulus) interpolation can be applied to establish that, at any location y in this region, the stress in the steel is determined as:

$$f_s=\frac{y f_y}{y_2}.$$

As shown in Figs. 10 and 11, y_1 is the distance from the top of the cross section to the PNA. For Case 1, $y_1 > D_{tube}$ (where D_{tube} is the outer diameter of the steel tube), and therefore the PNA is within the steel web. On the other hand, for Case 2, $y_1 < D_{tube}$, and the PNA is within the concrete filled tube infilled concrete. Both cases are considered hereafter.

Case 1. PNA in the web of the steel section ($y_1 \geq D_{tube}$)

In the compression zone, the forces can be divided into three regions, as shown in Fig. 10, represented by F_{c1}, which is the maximum compressive force in the concrete infill, F_{c2}, which is the compressive force in the steel tube and F_{c3}, which is the compressive force in the compressive region of the web. Each of these forces can be determined using Eqs. (16)–(18), respectively, where σ_c is the stress in the confined concrete obtained using Eq. (6) and r is the inner radius of the steel tube:

$$F_{c1}=2\int_{y_1-D_{tube}+t_t}^{y_1-t_t}\sqrt{r^2-(y-y_0)^2}\times\sigma_c\,dy \tag{21}$$

$$F_{c2}=2\left[\int_{y_2}^{y_1-t_t}\sqrt{R^2-(y-y_0)^2}-\sqrt{r^2-(y-y_0)^2}\times f_y dy+\int_{y_1-t_t}^{y_1}\sqrt{R^2-(y-y_0)^2}\times f_y dy+\int_{y_1-D_{tube}+t_t}^{y_2}\sqrt{R^2-(y-y_0)^2}-\sqrt{r^2-(y-y_0)^2}\times f_s dy+\int_{y_1-D_{tube}}^{y_1-D_{tube}+t_t}\sqrt{R^2-(y-y_0)^2}\times f_s dy\right] \tag{22}$$

$$F_{c3}=\frac{1}{2}t_w(y_1-D_{tube})\times\frac{f_y(y_1-D_{tube})}{y_2} \tag{23}$$

In the tension zone, below the PNA, the total force in the web in tension, F_{t1}, is determined as:

$$F_{t1}=\frac{1}{2}t_w y_2 f_y+t_w\times(h-y_1-y_2-t_f)\times f_y \tag{24}$$

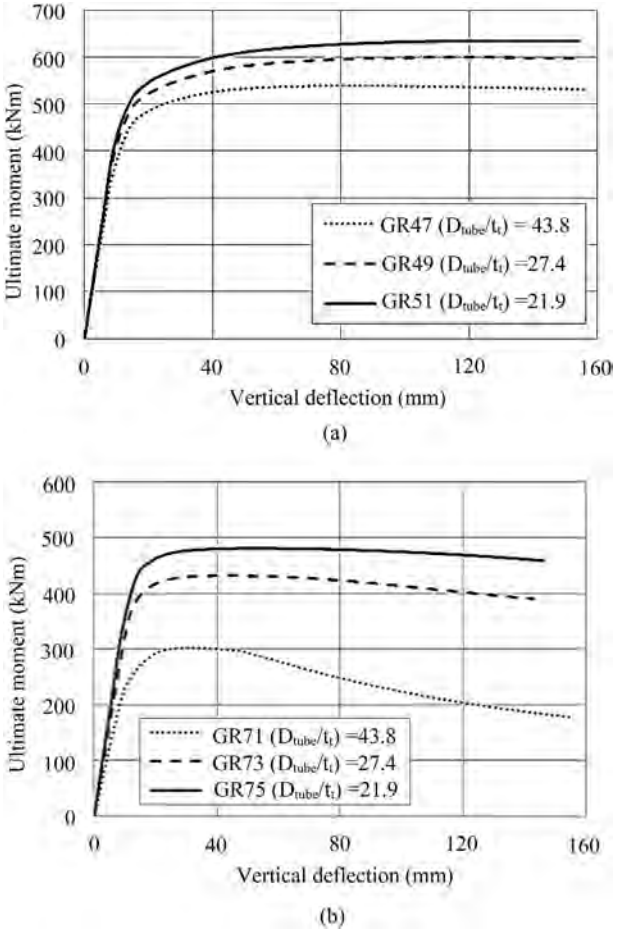

Fig. 14. Ultimate moment versus deflection responses of (a) CFTFGs (b) STFGs with different D_{tube}/t_t ratios.

On the other hand, the tensile force in the bottom flange is calculated as:

$$F_{t2} = b_f t_f f_y \tag{25}$$

Case 2. PNA is in the tubular flange ($y_1 \le D_{tube}$)

In this case, the total compressive force comprises two components, namely, F_{c1}, which is the force in the infilled concrete above the PNA and F_{c2}, which is force in the steel tube above the PNA. These are determined from Eqs. (26) and (27), respectively:

$$F_{c1} = 2\int_{0}^{y_1-t_t} \sqrt{r^2-(y-y_0)^2} \times \sigma_c \, dy \tag{26}$$

$$\begin{aligned} F_{c2} = 2 \times \Bigg[& \int_{y_2}^{y_1-t_t} \sqrt{R^2-(y-y_0)^2} - \sqrt{r^2-(y-y_0)^2} \times f_y dy \\ & + \int_{y_1-t_t}^{y_1} \sqrt{R^2-(y-y_0)^2} \times f_y dy + \int_{0}^{y_2} \sqrt{R^2-(y-y_0)^2} \\ & - \sqrt{r^2-(y-y_0)^2} \times f_s dy \Bigg] \end{aligned} \tag{27}$$

Below the PNA, there are three components to the total tensile force in the section. As can be seen in Fig. 11, y_1 bisects the steel tube, and the tensile force in the steel tube below the PNA (F_{t1}) is calculated as:

$$\begin{aligned} F_{t1} = 2 \times \Bigg[& \int_{-(D_{tube}-t_t-y_{1)}}^{0} \sqrt{R^2-(y-y_0)^2} - \sqrt{r^2-(y-y_0)^2} \\ & \times f_s dy + \int_{-(D_{tube}-y_{1)}}^{-(D_{tube}-t_t-y_{1)}} \sqrt{R^2-(y-y_0)^2} \times f_s dy \Bigg] \end{aligned} \tag{28}$$

Eq. (29) is used to calculate the tensile force for both the triangular and rectangular plastic stress distribution block areas of the steel web, below the PNA, as illustrated in Fig. 11:

$$F_{t2} = \int_{-y_2}^{y_1-D_{tube}} t_w \times f_s d_y + (h-y_1-y_2-t_f) \times t_w \times f_y \tag{29}$$

Finally, the tensile force in the bottom flange is:

$$F_{t3} = b_f t_f f_y \tag{30}$$

For both Case 1 and Case 2, F_{ci} ($i = 1, 2, 3, \ldots$, etc.) is any compressive force which exists above the PNA and F_{ti} ($i = 1, 2, 3, \ldots$, etc.) is any tensile force which exists below the PNA. C and T are the total compression and tension forces in the CFTFG, determined from:

$$C = \sum F_{ci} \tag{31}$$

and

$$T = \sum F_{ti} \tag{32}$$

In order to maintain equilibrium, the total compressive force (C) must equal the total tensile force (T) in the cross-section.

3.2. Ultimate moment capacity

For both cases described in the previous section, the ultimate bending capacity (M_u) for a CFTFG can be derived based on equilibrium of internal forces in the cross-section, as given in Eq. (33):

$$M_u = \sum M_{ci} + \sum M_{ti} \qquad (i = 1, 2, 3 \ldots \text{etc}) \tag{33}$$

The moment generated by the compressive and tensile forces (M_c and M_t, respectively) are found using Eqs. (34) and (35) for Case 1:

$$\begin{aligned} M_c = 2 \times \Bigg[& \int_{y_1-D_{tube}+t_t}^{y_1-t_t} \sqrt{r^2-(y-y_0)^2} \times \sigma_c \times y dy + \int_{y_2}^{y_1-t_t} \sqrt{R^2-(y-y_0)^2} \\ & - \sqrt{r^2-(y-y_0)^2} \times f_y \times y dy + \int_{y_1-t_t}^{y_1} \sqrt{R^2-(y-y_0)^2} \\ & \times f_y \times y dy + \int_{y_1-D_{tube}+t_t}^{y_2} \sqrt{R^2-(y-y_0)^2} - \sqrt{r^2-(y-y_0)^2} \\ & \times f_s \times y dy + \int_{y_1-D_{tube}}^{y_1-D_{tube}+t_t} \sqrt{R^2-(y-y_0)^2} \times f_s \times y dy \Bigg] \end{aligned} \tag{34}$$

$$\begin{aligned} M_t = & \frac{1}{2} t_w y_2 f_y \times \frac{2}{3} y_2 + t_w \times (h-y_1-y_2-t_f) \times f_y \\ & \times \frac{(h-y_1-y_2-t_f)}{2} + b_f t_f f_y \times \left(h-y_1-\frac{t_f}{2}\right) \end{aligned} \tag{35}$$

For Case 2, Eqs. (36) and (37) represent the moments above (M_c) and below (M_t) the PNA:

$$\begin{aligned} M_c = 2 \times \Bigg[& \int_{0}^{y_1-t_t} \sqrt{r^2-(y-y_0)^2} \times \sigma_c \times y dy + \int_{y_2}^{y_1-t_t} \sqrt{R^2-(y-y_0)^2} \\ & - \sqrt{r^2-(y-y_0)^2} \times f_y \times y dy + \int_{y_1-t_t}^{y_1} \sqrt{R^2-(y-y_0)^2} \times f_y \times y dy \\ & + \int_{0}^{y_2} \sqrt{R^2-(y-y_0)^2} - \sqrt{r^2-(y-y_0)^2} \times f_s \times y dy \Bigg] \end{aligned} \tag{36}$$

$$\begin{aligned} M_t = 2 \times \Bigg[& \int_{-(D_{tube}-t_t-y_{1)}}^{0} \sqrt{R^2-(y-y_0)^2} - \sqrt{r^2-(y-y_0)^2} \times f_s y dy \\ & + \int_{-(D_{tube}-y_{1)}}^{-(D_{tube}-t_t-y_{1)}} \sqrt{R^2-(y-y_0)^2} \times f_s \times y dy \\ & + \int_{-y_2}^{y_1-D_{tube}} t_w \times f_s \times y d_y + (h-y_1-y_2-t_f) \times t_w \\ & \times f_y \times (h-y_1-y_2-t_f) \Bigg] \end{aligned} \tag{37}$$

In order to check the validity of the proposed theoretical equations, Table 3 presents a comparison between the calculated ultimate moment capacity ($M_{u,Calc}$) and both the experimental value ($M_{u,Exp}$) [15] and the FE prediction using the model described previously ($M_{u,FE}$). For this beam, the PNA is found to be in the tubular part of the section and therefore the Case 2 formulations are used. The results show that the term y_1, which is the distance from the top of the steel beam to the PNA, is equal to 155.9 mm. It is clear from the table that the analytical expressions provide a good prediction of the moment capacity for this CFTFG. The

ratio of $M_{u,FE}$ to $M_{u,Exp}$ is 1.006 whereas the equivalent comparison of $M_{u,FE}$ and $M_{u,Calc}$ yields a ratio of 0.992.

4. Parametric study

As previously stated, the experimental data available for CFTFGs is limited to a single test [15], mainly owing to the expense associated with large-scale experiments as well as the novelty of these types of structural section. Therefore, a detailed analysis of the behaviour and performance criteria requires the use of numerical and/or analytical tools. In this section, the finite element model and analytical approach previously described are employed to investigate the ultimate behaviour of CFTFGs and the influence of the most salient parameters on their performance.

A number of parameters are investigated in the parametric study including geometrical and material details. In addition, FE models for steel tubular flange girders (STFGs) are generated in order to study the influence of the concrete infill on the behaviour. For CFTFGs, buckling takes place in the lateral-torsional mode as the web becomes stiffened transversally at the mid-span location, causing lateral buckling to dominate, rather than the web distortions; Fig. 12 shows the buckling mode of the tested girders. A total of 88 different arrangements are considered in this study, as presented in Tables 4–7. For clarity, in the current section, the results are presented in two general categories: (i) members with different tube diameters (Tables 4 and 5 for CFTFGs and STFGs, respectively) and (ii) beams with various tube thicknesses (Table 6 for CFTFGs and Table 7 for STFGs). In all cases, the webs of the girders are transversally stiffened with double-sided flat plate stiffeners which are 12 mm in thickness and located at the support and loading locations. The distance between the two intermediate stiffeners in the girder (a) is 1500 mm. All modelled beams had a length of 4300 mm. All specimens listed in Tables 4 and 6 contain concrete infill with a compressive strength of 38.6 MPa. In addition, combined yielding and torsional buckling is the failure mode for all models. This type of failure is common for these types of girders [20,21].

In the specimens listed in Tables 4 and 5, models with five different tube diameters (D_{tube} = 180, 200, 210, 219 and 300 mm) are considered. For each model, two web heights (h_w = 267 and 500 mm), giving two different panel aspect ratios (a/h_w = 5.62 and 3) and two flange thicknesses (t_f = 14 and 28 mm) are considered. The tube and web thicknesses are kept fixed at 8 mm and 6 mm, respectively.

In the specimens listed in Tables 6 and 7, models with three different tube thicknesses (t_t = 5, 8 and 10 mm) are considered. For each model, two different web heights (h_w = 267 and 500 mm) and two different web thicknesses (t_w = 6 and 10 mm), giving two different panel aspect ratios (a/h_w = 5.62 and 3) and four different web slenderness values ($\bar{\lambda}_w$ or h_w/t_w = 44.5, 26.7, 83.3 and 50), and two flange thicknesses (t_f = 14 and 28 mm) are considered. The tube diameter is kept fixed at 219 mm.

The ultimate moments determined using the FE model $M_{u,FE}$ and the analytical expressions $M_{u,Calc}$ are presented in Tables 4–7, together with the location of PNA measured from the top of the section (y_1). The results generally show that each pair of CFTFGs and STFGs (i.e. identical properties apart from the inclusion of concrete) has similar buckling shapes but the buckling load of the CFTFGs is higher than that of the corresponding STFGs. For example, the buckling loads of GR13 and GR33, which are a CFTFG and STFG, respectively, are 540.2 kNm and 391.2 kNm. This equates to a 38% increase in capacity due to the presence of concrete in the tube, which increases the strength and stiffness of the upper flange and hence allows the concrete filled section to carry additional loads.

On the other hand, as expected, girders with a relatively small web panel aspect ratio demonstrate significantly greater ultimate moment capacities compared with members with higher a/h_w ratios. From Tables 4 and 5, it is seen that the ultimate moment of GR15 is 842.5 kNm while for GR35 it is 650.8 kNm. These girders are identical to GR13 and GR33 previously discussed except that GR15 and GR35 have a web panel aspect ratio of 3 whereas GR13 and GR33 have an equivalent value of 5.62. The ultimate moment capacity is 56% greater for GR15 relative to GR13 whereas the same increase is 66% for GR35 compared with GR33. This demonstrates that irrespective of the presence of concrete, the aspect ratio of the web panel is highly influential to the load-bearing capacity of the girder.

In the following sub-sections, the load-deflection and failure behaviour of both CFTFGs and STFGs with different key parameters are presented and discussed in detail. Typically, each parameter is varied in isolation while the others are kept constant in order to study the effect of this term.

4.1. Effect of specimen geometry

In this section, the effect of a number of the most salient individual geometric properties such as tube diameter (D_{tube}), tube thickness (t_t) and tension flange thickness (t_f) are studied. Firstly, the influence of the diameter of the tubular flange (D_{tube}) is investigated by varying this dimension between 180 and 300 mm, while the thickness of the tube remains fixed at 8 mm. The moment-deflection results are presented in Fig. 13 for (a) CFTFGs and (b) STFGs, and it is evident that in both cases, increasing the diameter of the tubular flange raises the ultimate flexural strength of the girder. This is more significant for the concrete filled members compared with the bare steel sections owing to the increased strength and stiffness resulting from the concrete infill. There is some difference in the general shape of the curves presented in Fig. 13 with the concrete filled members showing a more rounded moment-deflection response with no softening whilst the STFGs demonstrate a descending branch after the peak moment has been reached, particularly for GR37. This is attributed to the fact that the concrete filled members do not experience local buckling even at high levels of deflection, due to the confinement effect provided by the concrete core. It is noteworthy that all of the sections in the current study were examined for local buckling using the requirement described in the AASHTO design specifications [38], and given as:

$$\frac{D_{tube}}{t_t} \le 2.8\sqrt{\frac{E}{f_y}} \tag{38}$$

Eq. (38) was originally developed based on an unfilled tube although the AASHTO specification recommends using the expression for concrete filled tubes also.

Fig. 14 presents the moment-deflection responses for (a) CFTFGs and (b) STFGs with different D_{tube}/t_t ratios and it is observed that decreasing the tube diameter to thickness ratio, by either reducing D_{tube} or increasing t_t, has the effect of increasing the moment capacity of the girders for both concrete filled and bare steel members. For the STFGs, this is expected as a lower D_{tube}/t_t ratio corresponds to a stockier compression flange, which is less susceptible to local buckling, and does not limit the cross-section flexural resistance of the compression flange. This effect is less prominent for the CFTFGs, as the confinement effect offered by the concrete infill has a greater effect in improving the local buckling resistance of the compression flange tube of all D_{tube}/t_t ratios. The ratio limits depend on the AASHTO design specifications [38], as given in Eq. (38).

In order to investigate the effect of plate thickness in the tension region of the cross-section on the behaviour, two different thicknesses of the bottom flange t_f are studied. The moment-deflection curves presented in Fig. 15 verify that, as expected, increasing the tensile flange thickness raises the ultimate moment capacity of the section. From a cost perspective (both materials and fabrication), it is important to consider whether the increased volume of steel required in GR64 compared to GR63, for example, is translated into improved moment capacity.

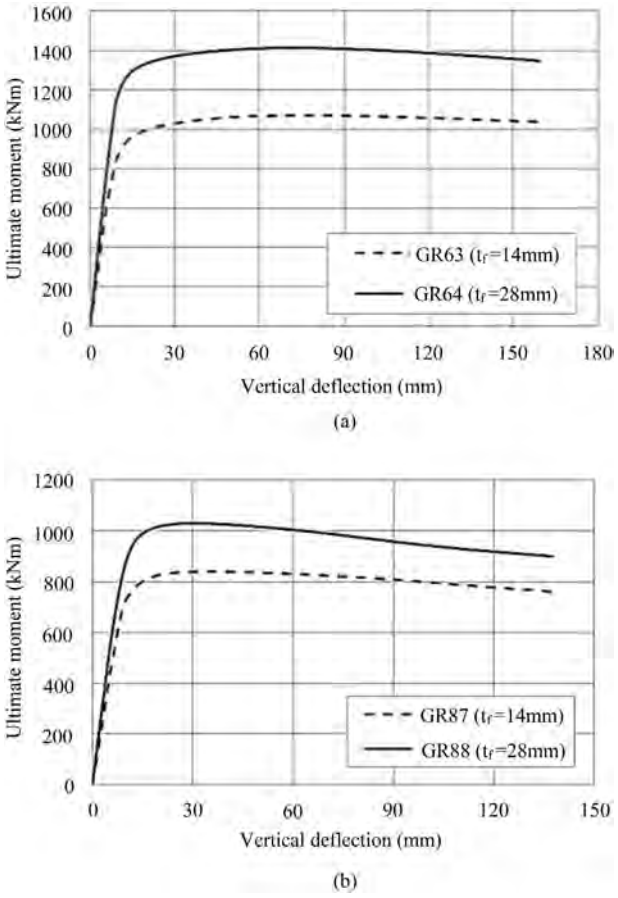

Fig. 15. Ultimate moment versus deflection responses for (a) CFTFGs (b) STFGs with different bottom flange thicknesses.

These two beams have an ultimate moment capacity of around 1413.2 kNm and 1069.4 kNm, respectively, and a gross cross-sectional area (steel only) of 11,901 and 9801 mm^2, respectively. Therefore, a 21% increase in steel volume can result in a 32% improvement in bending moment capacity, for the same stiffener arrangement. This effect is again examined in this section taking into account the web depth (h_w), which is a key parameter to consider in the design of plate girders. Clearly, decreasing the web depth (h_w) reduces the volume of steel in the section as well as the fabrication costs as less welding is required and the associated risk of weld distortion is lowered. However, it also reduces the bending moment capacity. Therefore, this discussion highlights the importance of a careful consideration of all factors (capacity requirements, flange depth, web depth, welding needs, etc.) when designing a CFTFG.

4.2. Effect of web panel aspect ratio

As previously observed in Tables 4–7, decreasing the aspect ratio of the web panels (a/h_w) for the same girder geometries leads to an increase in the ultimate moment capacity of the tubular flange girders. The ultimate moment-deflection curves for GR13 and GR15 are presented in Fig. 16 to illustrate the difference in their general behaviour. After the linear elastic stage, and until reaching the full strength of the girders, the girder with the higher web panel aspect ratio reaches the inelastic stress stage at a lower deflection relative to GR15 and also achieves a significantly higher moment capacity. This is attributed to the fact that GR13 (with the lower a/h_w ratio of these two beams) possesses a larger buckling resistance and also greater web stiffness, compared with GR15.

Fig. 17 presents the variation of $M_{u,FE}/M_{u,Calc}$ for different subgroups of CFTFGs and STFGs. Each subgroup represents girders with the same length and tube diameter, but other parameters such as h_w, t_f and a/h_w are varied. The results indicate the accuracy of the analytical expressions in predicting the ultimate moment as, in all cases, the $M_{u,FE}/M_{u,Calc}$ ratio is between 0.95 and 1.0. Moreover, the figures show that $M_{u,FE}$ and $M_{u,Calc}$ consistently become closer for members with a relatively large tube diameter and also a lower a/h_w ratio thus indicating the analytical expressions are most accurate in these cases. On the other hand, it can be seen that for both CFTFGs and STFGs, increasing the bottom flange thickness t_f results in the $M_{u,FE}/M_{u,Calc}$ ratio becoming closer to unity for all girders, irrespective of the web panel aspect ratio.

4.3. Effect of web plate slenderness

The effect of the web plate slenderness, that is the h_w/t_w ratio, is discussed herein. Fig. 18 displays the ultimate moment versus deflection response for (a) CFTFGs and (b) STFGs, for different web slenderness values. From the figures, together with the data presented in Tables 6 and 7, it is observed that increasing the web thickness (thereby reducing the h_w/t_w ratio) increases the moment capacity of the CFTFGs and STFGs, as expected, owing to the increased stiffness of the web plate. This is more pronounced in the concrete filled members (Fig. 18 (a)) compared with the bare steel flange girders (Fig. 18(b)). For example, the ultimate moment of GR55 (h_w/t_w = 83.3) is 842.5 kNm whereas the same value for GR61, which is identical apart from the thickness of the web plate (h_w/t_w = 50), is 1035.3 kNm. Thus, the increase in web thickness and hence reduction in web plate slenderness for concrete filled members, results in an improved moment capacity of almost 23%. The variation in web thickness from 6 mm to 10 mm increases the cross-sectional area of the section by around 17% (6404 mm^2 for GR55 to 7472 mm^2 for GR 61).

On the other hand, the same values for GR79 and GR85, which are identical to GR55 and GR61 apart from the absence of a concrete infill, are 650.8 and 722.3 kN, respectively, which represents an increase of only 11% for the same variation in web thickness, although the increase in steel volume remains at 17%. For the bare steel sections, although having a thicker web does increase the moment capacity of the section, this is limited to an 11% improvement as failure is likely to be affected by buckling in the top flange before any more capacity can be achieved. However, for the concrete filled members, buckling is extremely unlikely in the top flange owing to the stiffness provided by the concrete core, and therefore the increase in web thickness results in a much more significant improvement in the moment capacity. This illustrates the effect of the concrete infill in terms of overall behaviour and the

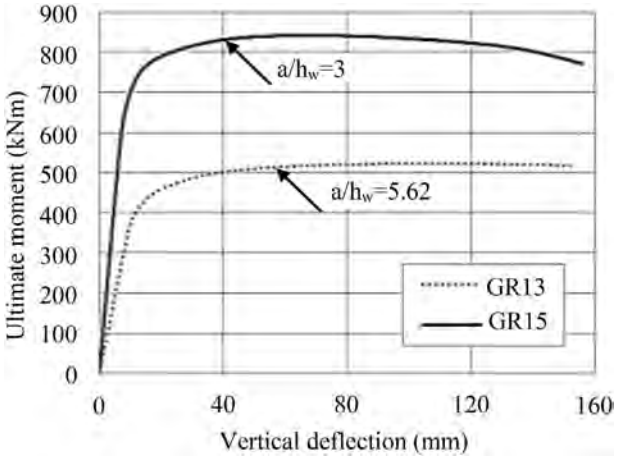

Fig. 16. Ultimate moment versus deflection for GR13 and GR15 with difference web panel aspect ratios.

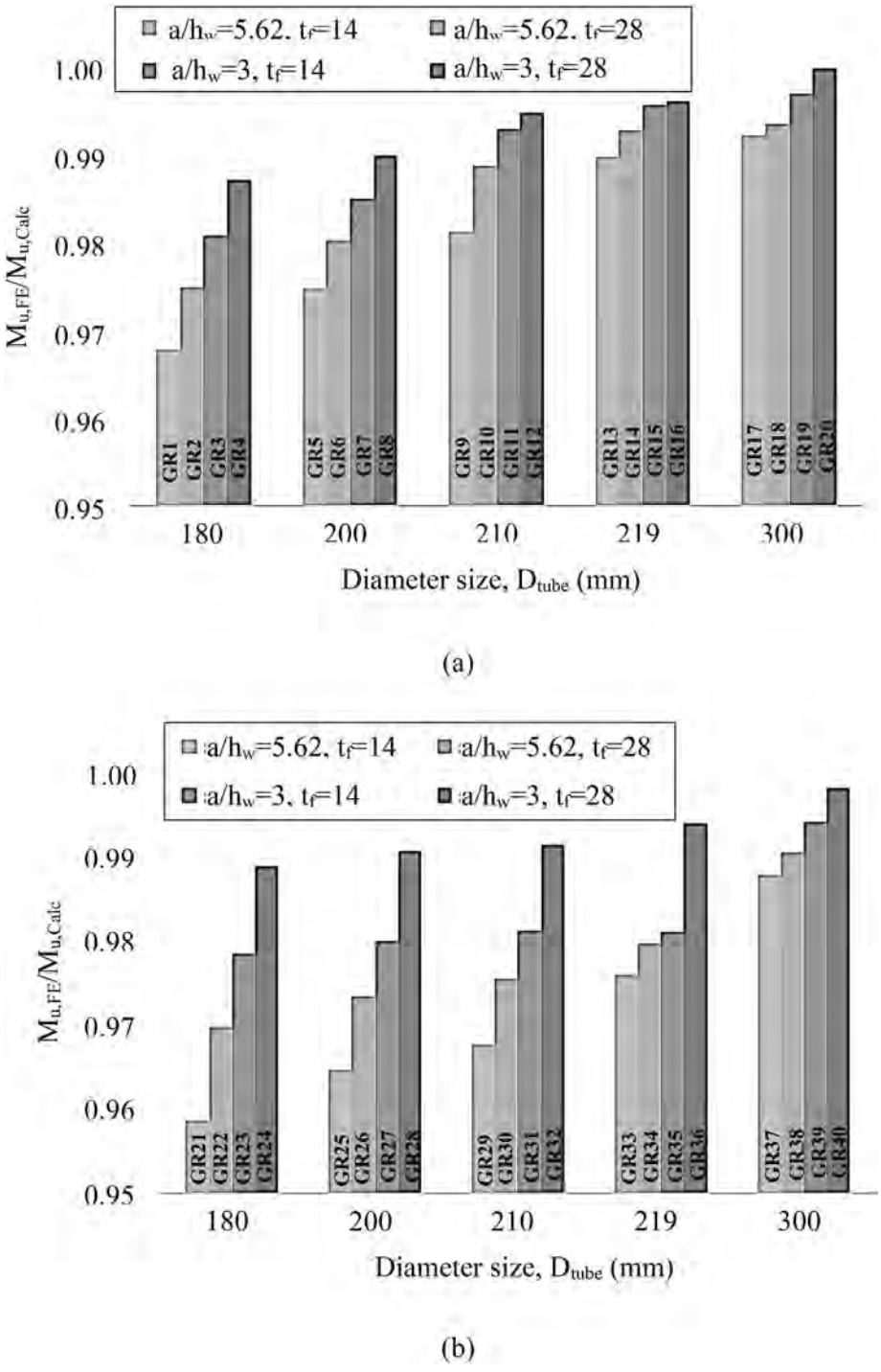

Fig. 17. The relationship between aspect ratio of the web panel (a/h_w) and the $M_{u,FE}/M_{u,Calc}$ ratio for (a) CFTFGs (b) STFGs.

stiffness provided can be more favourable even than increasing the amount of steel in the section.

4.4. Concrete compressive strength

The effect of concrete compressive strength on the response is investigated herein by considering different f_c values ranging from 20 to 70 MPa for specimen GR13, as presented in Table 8. The ultimate moment-displacement responses for these members are shown in Fig. 19. It can be seen that the value of f_c has a very slight effect on the capacity of the CFTFGs, which could be ignored. As expected, the moment capacity increases with greater concrete strengths and the PNA is located at a higher position in the cross-section. From the figure, it is observed that the concrete strength does not have a strong effect on the member rigidity during the elastic stage, where behaviour is controlled by the stiffness rather than strength. From the ratio of $M_{u,FE}$ to $M_{u,Calc}$, as presented in Table 8, it is clear that the analytical model provides a more accurate prediction of the moment capacity for relatively low values of f_c, which is expected owing to the diminished contribution made be the concrete in this case. Overall, it can be concluded that the increased strength of the CFTFGs compared to that of the STFGs is attributed to the availability of a rigid medium in the upper flange rather than the

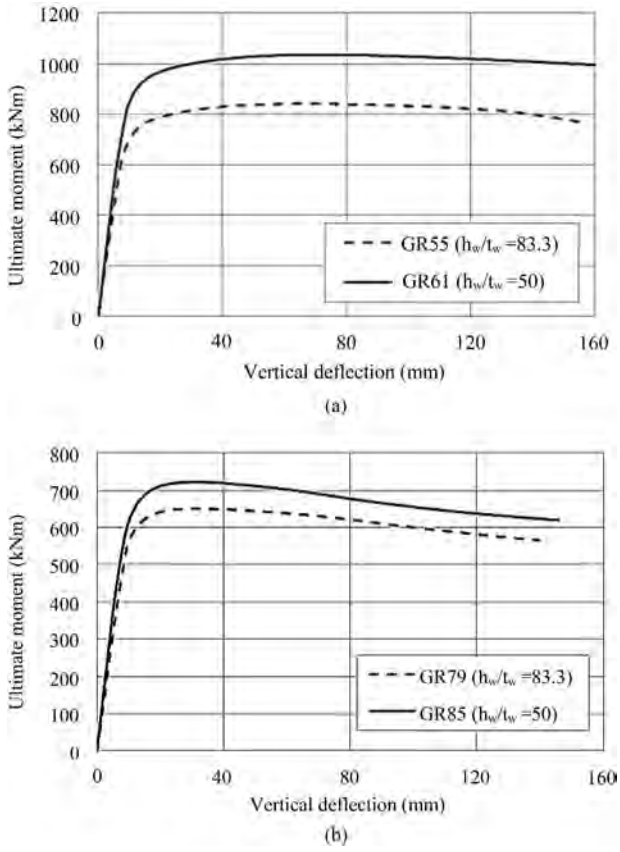

Fig. 18. Ultimate moment versus deflection responses of (a) CFTFGs (b) STFGs with different web plate slenderness' (h_w/t_w).

concrete strength, within the range examined herein. Accordingly, it is not necessary to include the compressive strength of the infill concrete in the design strength of the CFTFGs.

4.5. Steel strength

Fig. 20 presents the moment-displacement curves for the GR13 CFTFG but with different yield strengths of steel f_y. The details are also presented in Table 8, where it is seen that f_y was varied between 235 and 690 N/mm^2. Fig. 20 illustrates that the ultimate bending capacity is proportional to the yield strength of steel, as expected. Also, the steel strength makes almost no contribution to the stiffness of the member in the elastic stage, which is again expected as the Young's modulus value remains constant. The influence of steel strength on the $M_{u,FE}/M_{u,Calc}$ ratio is also provided in Table 8 and it can be seen that the members with higher steel strength also give greater $M_{u,FE}/M_{u,Calc}$ ratios, thus indicating that the analytical model captures the behaviour of these members particularly well.

Table 8
Influence of f_c and f_y on the capacity of CFTFG GR13.

f_c (MPa)	f_y (N/mm^2)	$M_{u,FE}$ (kNm)	$M_{u,Calc}$ (kNm)	PNA location (mm)	$M_{u,FE}/M_{u,Calc}$
20	287.9	525.5	526.0	168.8	0.999
30	287.9	536.5	539.8	161.2	0.993
38.6	287.9	540.2	544.6	155.9	0.992
40	287.9	545.8	550.9	155.1	0.990
50	287.9	553.1	562.7	150.1	0.983
60	287.9	558.2	569.1	145.9	0.981
70	287.9	561.8	575.6	142.3	0.976
38.6	235	433.7	442.7	154.1	0.978
38.6	355	631.4	638.0	157.6	0.988
38.6	460	799.3	803.1	159.7	0.995
38.6	690	1161.1	1162.4	162.4	0.998

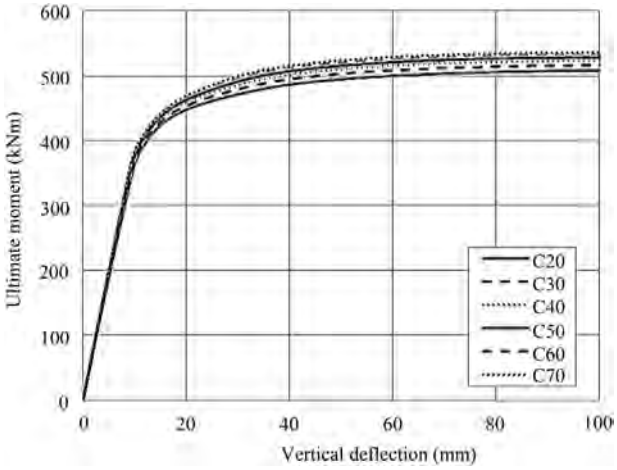

Fig. 19. Influence of concrete strength on the behaviour of CFTFGs.

5. Conclusions

This paper has presented a detailed investigation in the behaviour of concrete filled tubular flange girders (CFTFGs) under bending. In the absence of significant experimental testing in the literature, a finite element model was developed using the ABAQUS software [16] to study the response and also the relative influence of the most salient parameters. The accuracy of the FE models was initially assessed using the experimental results of Wang et al. [15], who conducted the only test on these members in the public domain, and it was shown that the proposed FE model is able to provide a very good prediction of the general behaviour and the ultimate capacity. In addition to the numerical model, an analytical model was also developed and discussed, which predicts the bending capacity of these members based on a plastic analysis approach. The analytical approach was validated using both the experimental data available as well as the FE model.

Thereafter, parametric studies were conducted to study the relative influence of several key parameters including the size of the tube diameter (D_{tube}), the ratio of D_{tube} to the tube thickness, the thickness of the bottom flange, the web plate slenderness, the aspect ratio of the web panel and also the material strengths. Ultimate moment versus vertical deflection curves and failure modes were obtained from the analyses. For comparison purposes, steel tubular flange girders (STFGs) were also assessed. Based on this parametric study, the following conclusions can be made:

1. Each pair of CFTFGs and STFGs with identical properties apart from the presence of concrete were found to have similar buckling shapes with the buckling load of the CFTFGs being higher than that of the corresponding STFGs. This highlights the influence of the infill concrete which increases the stiffness of the upper flange, and hence allows the section to carry additional ultimate moment capacity compared to the STFGs.
2. The flexural strengths predicted using the proposed analytical expressions were shown to give an accurate, yet conservative, depiction of the capacity for both CFTFGs and STFGs.
3. In terms of the geometrical details, it was shown that increasing the bottom flange depth (t_f) or the thickness of the tubular section (t_t) is advantageous both in terms of moment capacity achieved and also the material costs. This is because the increase in moment capacity

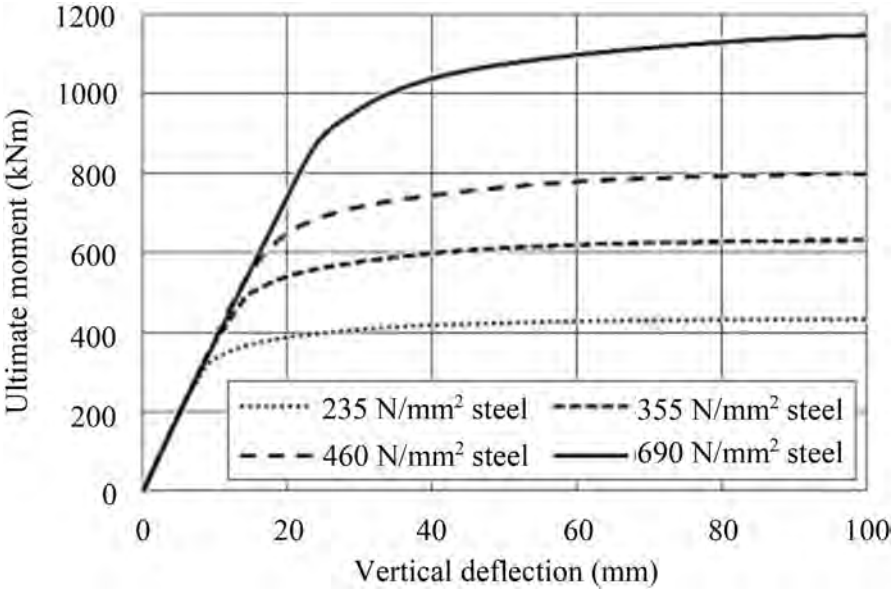

Fig. 20. Vertical deflection at mid-span section with different yielding strength of steel.

achieved is disproportionately large, compared with the increase in the cross-sectional area.

4. It was clearly demonstrated that decreasing the aspect ratio of the web panel (a/h_w) results in an increase in the flexural strength of the girders. Such an increase is more pronounced for CFTFGs compared to STFGs.
5. The concrete compressive strength (f_c) was shown to have almost no effect on the strength and behaviour of CFTFGs. Hence, the improved strength of CFTFGs compared to that of equivalent STFGs is attributed to the availability of a rigid concrete medium in the tubular flange. On the other hand, the yield strength of the steel does contribute to the ultimate bending capacity of the girders.
6. Finally, based on the absence of specific flexural design formulae for the CFTFGs in Eurocode 4 [39], a design model providing suitable ultimate moment capacity values predictions for CFTFGs has been presented. This model is based on a fundamental assessment of the behaviour, capturing the relative influence of important material and geometric parameters and has been shown to provide an accurate prediction of the load bearing capacity of CFTFGs.

Acknowledgments

The authors would like to gratefully acknowledge the financial support by the Office of the Prime Minister of Iraq through the Higher Committee for Education Development in Iraq.

References

[1] W.G. Wassef, P.A. Ritchie, J.M. Kulicki, Girders with corrugated webs and tubular flanges—An innovative bridge system, Proceedings of the 14th Annual Meeting, International Bridge Conference, Pittsburgh, USA, 1997.
[2] Y.L. Pi, N.S. Trahair, Lateral-distortional buckling of hollow flange beams, J. Struct. Eng. 123 (6) (1997 Jun) 695–702.
[3] P. Avery, M. Mahendran, Finite-element analysis of hollow flange beams with web stiffeners, J. Struct. Eng. 123 (9) (1997 Sep) 1123–1129.
[4] C.W. Kurniawan, M. Mahendran, Elastic lateral buckling of simply supported LiteSteel beams subject to transverse loading, Thin-Walled Struct. 47 (1) (2009) 109–119.
[5] T. Anapayan, M. Mahendran, D. Mahaarachchi, Lateral distortional buckling tests of a new hollow flange channel beam, Thin-Walled Struct. 49 (1) (2011) 13–25.
[6] M.F. Hassanein, O.F. Kharoob, Shear strength and behavior of transversely stiffened tubular flange plate girders, Eng. Struct. 32 (9) (2010 Sep 1) 2617–2630.
[7] M.F. Hassanein, O.F. Kharoob, An extended evaluation for the shear behavior of hollow tubular flange plate girders, Thin-Walled Struct. 56 (2012) 88–102.
[8] M.F. Hassanein, O.F. Kharoob, A.M. El Hadidy, Lateral–torsional buckling of hollow tubular flange plate girders with slender stiffened webs, Thin-Walled Struct. 65 (2013) 49–61.
[9] M.F. Hassanein, N. Silvestre, Lateral–distortional buckling of hollow tubular flange plate girders with slender unstiffened webs, Eng. Struct. 56 (2013 Nov 1) 572–584.
[10] M.R. Wimer, R. Sause, Rectangular tubular flange girders with corrugated and flat webs, ATLSS Report 04–18, ATLSS Engineering Research Center, Lehigh University, 2004.
[11] R. Sause, B.G. Kim, M.R. Wimer, Experimental study of tubular flange girders, J. Struct. Eng. 134 (3) (2008 Mar) 384–392.
[12] B.G. Kim, R. Sause, Lateral torsional buckling strength of tubular flange girders, J. Struct. Eng. 134 (6) (2008 Jun) 902–910.
[13] F. Gao, H.P. Zhu, D.H. Zhang, T.S. Fang, Experimental investigation on flexural behavior of concrete filled pentagonal flange beam under concentrated loading, Thin-Walled Struct. 84 (2014) 214–225.
[14] R. Sause, Innovative steel bridge girders with tubular flanges, Struct. Infrastruct. Eng. 11 (4) (2015 Apr 3) 450–465.
[15] C.S. Wang, X.L. Zhai, L. Duan, B.R. Li, Flexural limit load capacity test and analysis for steel and concrete composite beams with tubular up-flanges, Proceedings of the 12th International Symposium on Tubular Structures, Shanghai, China, 2008.
[16] ABAQUS 6.14-4, Waltham, MA, Dassault Systèmes, 2011.
[17] E. CEN, 1090-2: Execution of Steel Structures and Aluminium Structures–Part 2: Technical Requirements for Steel Structures, European Committee for Standardisation, Brussels, 2008.
[18] AISC, Manual of Steel Construction – Load and Resistance Factor Design, 2nd ed., 1998 Chicago.
[19] AISC, Load and Resistance Factor Design Specification, for Structural Steel Buildings, American Institute of Steel Construction, Chicago, 1999.
[20] M.F. Hassanein, Fundamental behaviour of concrete-filled pentagonal flange plate girders under shear, Thin-Walled Struct. 95 (2015 Oct 1) 221–230.
[21] B.G. Kim, R. Sause, High performance steel girders with tubular flanges, ATLSS Report 05–15, ATLSS Engineering Research Center, Lehigh University, Bethlehem (PA, USA), 2005.
[22] Y. Ding, Y. Zhang, J. Zhao, Tests of hysteretic behavior for unbonded steel plate brace encased in reinforced concrete panel, J. Constr. Steel Res. 65 (5) (2009 May 1) 1160–1170.
[23] EN 1992-1-1, Eurocode 2: Design of Concrete Structures: Part 1–1: General Rules and Rules for Buildings, CEN, 2004.
[24] H.T. Hu, C.S. Huang, M.H. Wu, Y.M. Wu, Nonlinear analysis of axially loaded concrete-filled tube columns with confinement effect, J. Struct. Eng. 129 (10) (2003 Oct) 1322–1329.
[25] S.H. Lee, B. Uy, S.H. Kim, Y.H. Choi, S.M. Choi, Behavior of high-strength circular concrete-filled steel tubular (CFST) column under eccentric loading, J. Constr. Steel Res. 67 (1) (2011 Jan 1) 1–3.
[26] E. Ellobody, Numerical modelling of fibre reinforced concrete-filled stainless steel tubular columns, Thin-Walled Struct. 63 (2013 Feb 1) 1–2.
[27] J.B. Mander, M.J. Priestley, R. Park, Theoretical stress-strain model for confined concrete, J. Struct. Eng. 114 (8) (1988 Aug) 1804–1826.
[28] F.E. Richart, A. Brandtzaeg, R.L. Brown, A Study of the Failure of Concrete Under Combined Compressive Stresses, University of Illinois at Urbana Champaign, College of Engineering. Engineering Experiment Station, 1928.
[29] C.D. Goode, D. Lam, Concrete-filled steel tube columns-tests compared with Eurocode 4, Composite Construction in Steel and Concrete VI 2011, pp. 317–325.

[30] L.P. Saenz, Equation for the stress-strain curve of concrete, ACI J. 61 (9) (1964) 1229–1235.
[31] H.T. Hu, W.C. Schnobrich, Constitutive modeling of concrete by using nonassociated plasticity, J. Mater. Civ. Eng. 1 (4) (1989 Nov) 199–216.
[32] G. Giakoumelis, D. Lam, Axial capacity of circular concrete-filled tube columns, J. Constr. Steel Res. 60 (7) (2004 Jul 1) 1049–1068.
[33] E. Ellobody, B. Young, D. Lam, Behaviour of normal and high strength concrete-filled compact steel tube circular stub columns, J. Constr. Steel Res. 62 (7) (2006 Jul 1) 706–715.
[34] E. Ellobody, B. Young, Nonlinear analysis of concrete filled steel SHS and RHS columns, Thin-Walled Struct. 44 (8) (2006) 919–930.
[35] P. Kmiecik, M. Kamiński, Modelling of reinforced concrete structures and composite structures with concrete strength degradation taken into consideration, Arch. Civil Mech. Eng. 11 (3) (2011 Jan 1) 623–636.
[36] H. Ban, M.A. Bradford, Flexural behaviour of composite beams with high strength steel, Eng. Struct. 56 (2013 Nov 1) 1130–1141.
[37] J. Dong, R. Sause, Flexural strength of tubular flange girders, J. Constr. Steel Res. 65 (3) (2009 Mar 1) 622–630.
[38] AASHTO LRFD, Bridge Design Specifications, American Association of State Highway and Transportation Officials, Washington, DC, 1998.
[39] EN1994-1-1, Eurocode 4: Design of Composite Steel and Concrete Structures. Part 1-1: General Rules and Rules for Buildings, CEN, 2004.